Int J Adv Manuf Technol (2017) 88:303–316
DOI 10.1007/s00170-016-8757-3

ORIGINAL ARTICLE

Assessment of replication fidelity of optical microstructures by hot embossing

Giuseppe A. Cirino[1,2] · **Renê M. Granado**[3] · **Tayeb Mohammed-Brahim**[2] · **Renato G. Jasinevicius**[4]

Received: 13 November 2015 / Accepted: 8 April 2016 / Published online: 23 April 2016

Abstract This work reports the performance evaluation of low-cost hot embossing processes of fine three-dimensional microstructures, namely (i) cylindrical microlens array, (ii) plano-convex aspheric Fresnel lens, and (iii) pyramidal array structures. All those optical elements were replicated by employing a low-cost hot embossing tool in optical quality acrylic material. Scanning electron microscopy and optical interference microscopy techniques were used to quantitatively measure the obtained structures. In terms of the replication fidelity with respect to the mold counterpart, the resulting optical elements presented at least 96 % of dimensional fidelity at micro- and nanometer scale, including the structures with sharp edges present in the Fresnel lens. In terms of the surface optical quality, resulting root mean square surface roughness of at least one tenth of wavelength was obtained, considering applications in the visible range of spectrum. The results showed that even nanostructures generated by the material removal mechanisms during mold fabrication, such as crystal grain elastic recovery, were well replicated with differences in the range of few of nanometers which is within the vertical resolution of the employed optical interference technique.

✉ Giuseppe A. Cirino
gcirino@ufscar.br

[1] Departamento de Engenharia Elétrica, Universidade Federal de São Carlos, CEP 13560-905 São Carlos, São Paulo, Brazil

[2] IETR, Université de Rennes1, 35042 Rennes Cedex, France

[3] Instituto de Matemática e Estatística - CTC-UERJ, CEP 20550-013 Rio de Janeiro, Brazil

[4] Laboratório de Engenharia de Precisão, Departamento de Engenharia Mecânica, Escola de Engenharia de São Carlos, Universidade de São Paulo, C.P. 359, CEP 13566-590 São Carlos, São Paulo, Brazil

Keywords Diamond turning · Hot embossing · Diffractive optics · Wavefront sensor · PMMA replication fidelity · Aspheric Fresnel lens

1 Introduction

Micro-optical elements such as microlens arrays (MLA) and aspheric Fresnel lenses are typical example of parts that demand micro-fabrication technology involving their fabrication and subsequent replication for mass production purposes. Mechanical micro machining processes such as single-point diamond turning and milling are considered key manufacturing techniques to produce the mold inserts for these devices. Other technologies based on silicon processing are also important and available for micro-device fabrication. Since many of these direct fabrication processes are too expensive and time consuming for individual part manufacturing in large volume, replication on polymeric materials become a strong demand. Therefore, replication processes have become the most effective methods for producing large quantities, inexpensive micro parts due to its reduced cost process and small amount of polymeric material required.

There are many ways for replicating these components, enabling high volume manufacture of polymeric micro parts, such as micro injection molding, hot embossing, reaction injection molding, and thermoforming [1]. Hung et al. employed a micro-hot embossing system to fabricate UV-cured SU-8 aspheric lenses, by using nickel micro-electroforming and molding to achieve low-stress, low-surface roughness optical parts [2]. Sul et al. employed silicon substrate with microstructures patterned on its surface via wet etching, acting as mold insert, aiming the replication on polycarbonate. They adapted injection molding process to micro-fabrication, targeting micro-electro-mechanical-systems

(MEMS) applications [3]. Metwally and co-workers replicated 18-nm-wide groove polymeric structures from silicon dioxide master. They highlighted the influence of several effects on replication tool aiming a good quality replicated part, such as interfacial and tool surface effects, equipment response time, and high shear stress caused by thin walls and high filling pressures are important issues. For prototyping, they also mentioned the possibility to use silicon wafers or polymeric micro tool inserts or a combination of both [4–6].

The optical properties of polymethylmethacrylate (PMMA) microstructured lightguiding plates, with feature size ranging from 100 to 300 μm, fabricated by micro injection-compression molding was investigated by Shen et al. They found that the most significant process parameters for optical properties on micro injection molding are the mold temperature, melt temperature, and packing pressure [7]. Shan et al. reported the development of a micro-hot embossing process for high-quality PMMA micromirrors targeting optical switch applications. They highlighted that the way of filling the tiny cavities, maintaining the vertical sidewall surfaces, can be achieved by adopting a combination of a temperature of 185 °C and a pressure of 1.7 kg/mm^2 [8]. Lee et al. investigated the effects of processing conditions on the replication of PMMA microlens arrays by injection molding. They reported that the flow rate, packing pressure, and packing time are key factors that affect the replication quality. Best results, with average surface roughness of 1.6 nm, were found for high packing pressure of 20 MPa or high flow rate of 24 cm^3/s. Packing time was found to have little effect on the replication quality of microlens arrays [9].

Huang reported replication of high-quality nanostructures of 25 nm by using silicon-based mold insert. The key parameters to obtaining a clear structural definition were by keeping high mold temperature and with evacuation of the mold [10]. Hatori and co-workers suggested a modified injection system for molding of high-aspect-ratio nanostructures, where a nanostructured mold surface was heated during polymer filling and then immediately cooled by the mold bases, which are kept at a lower temperature. Using polystyrene, they demonstrated the replication of line-and-space (pitch 800 nm, depth 400 nm) and cone patterns (pitch 200 nm, depth 400 nm) with a cycle time of less than 15 s [11]. To achieve high aspect ratios over wafer-scale areas of polycarbonate (PC) and PMMA nanostructures, the critical parameters prove to be the embossing tool surface quality (sidewall roughness and angles) as well as the process temperature cycle and the chemical interface between master and substrate [12].

Numerical investigations of the flow behavior of polymer melting in micro-cavities by using finite element analysis have also been reported. Key factors affecting the flow behavior in micro injection molding, such as melting temperature, glass transition temperature, and molecular weight were studied. The authors found that injection time is the most important factor affecting part quality [13].

In this paper, three different optical micro-elements were fabricated by a hot embossing technique, aiming to show the high fidelity of the replication in the nanometric scale. The first optical device is a concentric, closed-loop cylindrical microlens array (denoted as Cyl-MLA), the second optical element is a millimeter-size plane-convex aspheric Fresnel lens (denoted as Fr-Lens), and the third one is a pyramidal array microstructure (denoted as Pyr-Array).

A low-cost home-built embossing system was employed, which makes possible to prototype and carry out preliminary tests on micro-optic elements in terms of mold insert machining strategy, replication fidelity, and optical performance on an affordable and fast ways. This would directly impact on the time to market of a new product.

The mold insert fabrication processes of each of the optical elements are detailed. The performance of the replication in PMMA of fine three-dimensional microstructures was quantitatively evaluated, by comparing dimensional measurements between molds and replicas.

Section 2 presents experimental details of the materials, manufacturing equipment, and characterization technique employed in this article. It also brings the design of the proposed micro-optical components, as well as details on the mold insert manufacturing, replication process, and replication apparatus. Section 3 reports the results and discussion for the fabrication of each of the polymeric micro-optical elements proposed in this work. Finally, in section 4, the conclusions are outlined.

2 Experimental details

2.1 Materials, manufacturing equipment, and characterization technique

Concerning the two optical elements, the Cyl-MLA and the Fr-Lens were fabricated by using ultraprecision single-point diamond turning machine, namely Rank Pneumo Model ASG 2500 (Aspheric Surface Generator). It comprises a T-base carriage configuration and carriages (hydrostatic bearing) driven by pulse-width-modulated dc-servomotors, rotary-to-linear motion through 5-mm pitch ballscrews, and position feedback using laser interferometer. It is equipped with computer numerical control, Allen-Bradley 8200 CNC model. The machine is mounted on a cast iron base, thermally stress-free, and isolated from external vibration by means of air-mounted passive isolators assembled on a steel frame. The spindle is supported by aerostatic bearings that provide high axial stiffness. Laser interferometric transducers monitor the axis positioning within 10-nm resolution. The third element proposed (Pyr-Array) was fabricated by imprinting in hardened steel with a pyramidal Vickers. The micro indenter

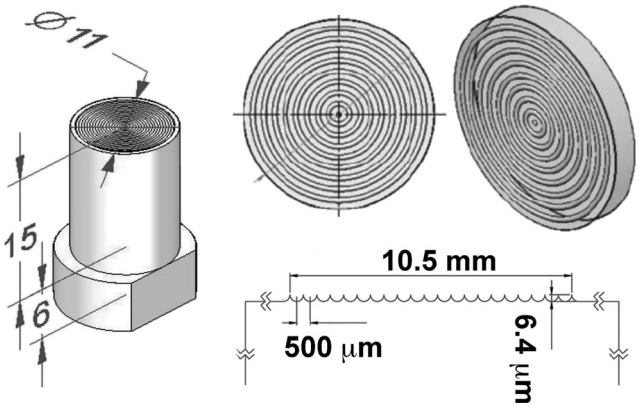

Fig. 1 Schematic view of concentric closed-loop cylindrical microlens array (Cyl-MLA) optical element with its key dimensional features

equipment used was a Leica Mikrosysteme Model VMHT MET (A-1170).

Both Cyl-MLA and Fr-Lens mold inserts were fabricated on commercially available non-ferrous 99.9 % purity electroless copper workpiece. Although copper is not suitable for mass production, it can be used in the prototyping stage. After prototype validation, it can be used as a seed for an electroformed harder material such as nickel, which can withstand large production cycles. By applying the electroformation method on nickel, for example, the precision of the electroplated negative insert could change. However, it is well known that the electroformation fidelity can be of molecular level [14]. Furthermore, this issue depends on the application. When one deals with optical micro-devices, it is important to compare the surface roughness and dimensional changes with respect to the operating wavelength (or wavelength range). In this case, where the optical micro-devices will operate at the visible range of the spectrum (400–700-nm wavelength range), the mold insert dimensional change induced by electroplating would have a relatively weak impact with respect to the device's performance.

The characterization of the resulting machined and replicated structures was performed by employing a non-contact optical profilometry technique. A Wyko NT 1100 system (Veeco Instruments, Inc) was used to measure the morphology and surface finish. The vertical-shifting interferometry (VSI) mode was chosen in these experiments. The vertical measurement range of this instrument is 0.1 nm to 1 mm and the lateral spatial sampling 0.08 to 13.1 μm. The surface profiles were then plotted and analyzed by Vision® software (also from Veeco).

The optical elements were replicated on PMMA, whose trade name is Plexiglas® V825, manufactured by Altuglas International.

2.2 Optical elements design

2.2.1 Concentric closed-loop Cyl-MLA design

The Cyl-MLA consists of ten lenses plus the center lens, as schematically depicted in Fig. 1. Each lens of the array present a diameter of $d = 500$ μm and a maximum height $h_{MAX} = 6.4$ μm, resulting in a focal length $f_L = 2.5$ mm and *f*-number $f/\# = (f_L/d) = 5$. The whole device has diameter of $D_L = 10.5$ mm.

The Cyl-MLA can be applied to a wavefront sensor based on Hartmann-Shack principle [15]. Typically, the MLA of a wavefront sensor has a rectangular distribution, which generates a discrete point-like intensity light pattern within its back focal plane. In this case, a circular symmetry is employed—in contrast to the conventional Cartesian symmetry of the MLA configuration—which generates a continuous circular-like intensity light pattern within its back focal plane. It was demonstrated that sensors of different symmetries and/or configurations could be tested and analyzed in order to quantify and compare their effectiveness when applied to visual optics [16].

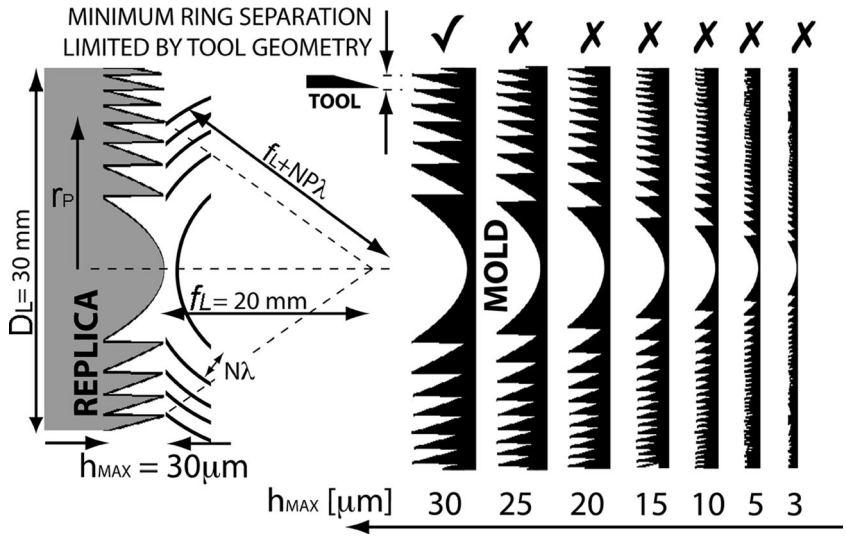

Fig. 2 Schematic view of the replica and mold. h_{MAX} is determined as a function of the tool geometry. In this case, the minimum $h_{MAX} = 30$ μm

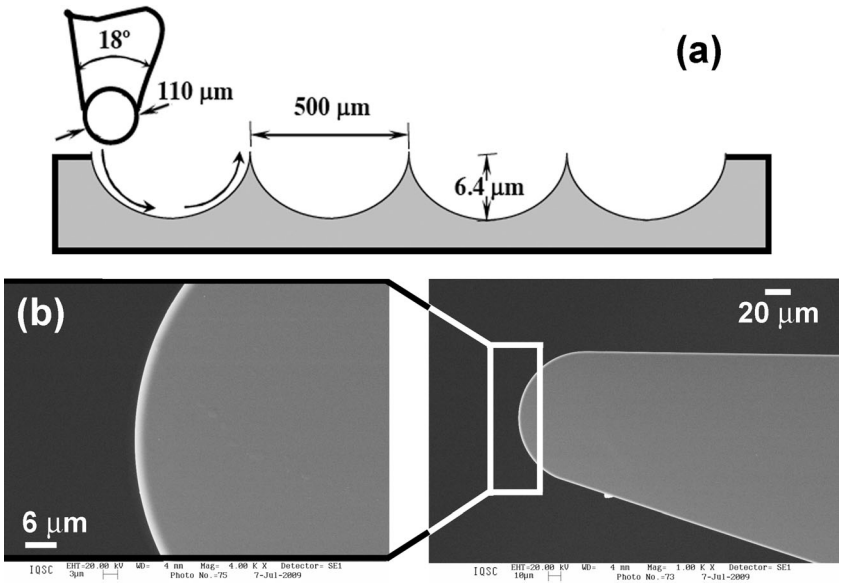

Fig. 3 **a** Schematic diagram of the machined surface generation of Cyl-MLA optical element using a round nose tool geometry. **b** Diamond tool geometry used to fabricate the Cyl-MLA optical element (single crystal diamond tool, from Contour Fine Tooling®, SCO 0.05 mLGC model, 55 μm nose radius, 0° rake angle and 10° clearance angle)

2.2.2 Aspheric Fr-Lens design

The second type of optical test structure is a millimeter-size convergent aspheric Fresnel lens. In this kind of lens, the annular rings are designed such that the optical path lengths for the light refracted from adjacent zones toward a common focal point differ by an integer multiple of a design wavelength. The lens was designed to have a diameter $D_L = 3$ mm and a focal length $f_L = 20$ mm, with a corresponding *f*-number *f*/# = 6.67.

The complex-valued thin converging lens optical transmittance, t_L, has a phase distribution, generated by using paraxial approximation with a quadratic phase factor given by [17, 18]

$$t_L(x,y) = \exp[j\phi_L(x,y)] = \exp\left[-j\frac{k}{2f_L}\left(x^2+y^2\right)\right] \quad (1)$$

where (x,y) is the two-dimensional coordinates of the lens, f_L is its focal distance, $k = (2\pi/\lambda)$ is the wave number, $\varphi_L(x,y)$ is the lens' phase modulation function, and λ is the operating wavelength. In order to implement a diffractive version of the lens, the phase function $\varphi_L(x,y)$ is wrapped to an interval between 0 and an integer multiple of 2π, given by

$$\phi_{N2\pi}(x,y) = [\phi_L(x,y)] \mathrm{mod} N.2\pi \quad (2)$$

where $\varphi_{N2\pi}(x,y)$ is the wrapped phase function $(0 < \varphi_{N2\pi} < N2\pi)$ and N is a positive integer, being determined by the specific fabrication method.

Table 1 Summary of the experimental conditions and tool geometry used for the Cyl-MLA mold insert fabrication

Concentric closed-loop MLA (Cyl-MLA)	
Cutting tool	
Material (Contour Fine Tooling®)	Mono-crystalline diamond
Nose radius (μm)	55
Rake	0°
Clearance (primary)	10°
Include angle	18°
Waviness <250 nm over 160° excluding elliptical form	
Workpiece	Electroless cooper
Cutting conditions	
Spindle speed (rpm)	1000
Feed rate (μm/rev)	1.0
Depth of cut (μm)	6.4 (max.)
Machining equipment	
Rank Pneumo model	Aspheric Surface Generator ASG 2500
Position resolution (nm)	10

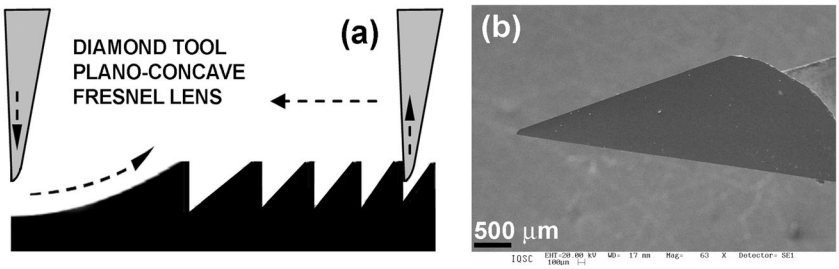

Fig. 4 **a** Machining strategy applied to the fabrication of the Fr-Lens mold insert. **b** SEM of the single-point diamond half radius tool used to machine the Fresnel mold cavity (single crystal diamond tool, from Contour Fine Tooling®, HCO 10 m LGC model, 115-μm nose radius, 0° rake angle and 10° clearance angle)

Table 2 Summary of the experimental conditions and tool geometry used for the Fr-Lens mold insert fabrication

Fresnel lens (Fr-Lens)	
Cutting tool	
Material (Contour Fine Tooling®)	Mono-crystalline diamond
Nose radius (μm)	115
Rake	0°
Clearance (primary)	10°
Include angle	30°
Waviness <250 nm over 160° excluding elliptical form	
Workpiece	Electroless cooper
Cutting conditions	
Spindle speed (rpm)	1000
Feed rate (μm/rev)	1.0
Depth of cut (μm)	Five-values strategy: 10 / 10 / 5 / 3 / 2
Machining equipment	
Rank Pneumo model	Aspheric Surface Generator ASG 2500
Position resolution (nm)	10

Since the annular period of the Fresnel lens increases by a square factor as a function of the distance from its center toward the periphery [18], it is necessary to establish the parameter N in such a way to obtain a satisfactory lens quality at the most peripheral ring for a given fabrication process.

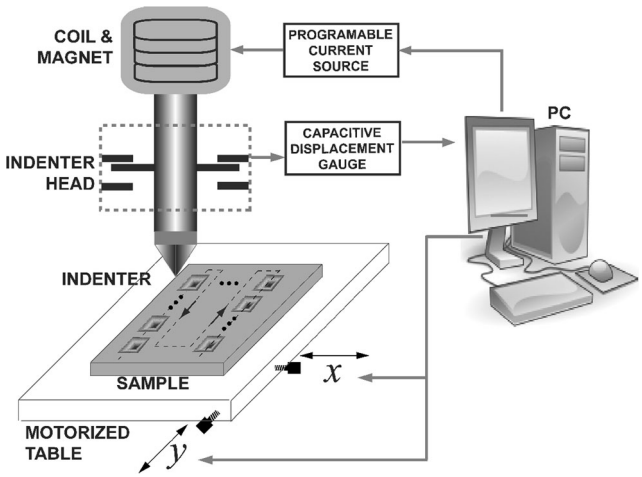

Fig. 5 Schematic view of the indentation equipment, with the controlled parts, as well as the indentation strategy for the generation of the Pyr-Array optical element. Pitch is 100 μm

The maximum height of the Fresnel lens, h_{MAX}, depends on N, and on the material, the lens is fabricated, being given by [1]

$$h_{MAX} = N\frac{\lambda}{n_{PMMA}-1} \tag{3}$$

where n_{PMMA} is the refractive index of PMMA at the wavelength λ.

Previous test showed that for the tool used in machining the Fresnel structures, a suitable fabrication process can be achieved with $h_{MAX} \geq 30$ μm.

Figure 2 illustrates schematically the criterion to choose h_{MAX}, as a function of the tool geometry, which allows a good optical element to be resolved in its periphery. In this case, the minimum $h_{MAX} = 30$ μm. For optical characterization purposes, in this case, λ was chosen to be approximately in the center of the visible spectrum $\lambda = 500$ nm and $n_{PMMA} = 1.5$. By setting the above values and $h_{MAX} = 30$ μm in Eq. 3, one obtains $N = 30$. This figure also shows the radius of the Pth ring of the Fresnel lens, r_P

Table 3 Summary of the experimental conditions for the Pyr-Array mold insert fabrication

Micro-pyramid optical element (Pyr-Array)	
Workpiece	VND steel tempered
Indentation conditions	
Load (gf)	1000
Load pressure (kg f/mm^2)	815
Indentation cycle (s)	15
Penetration speed (μm/s)	60
Indentation equipment	
Leica Mikrosysteme Model	VMHT MET Leica (A-1170)

Among the several applications of aspheric Fresnel lenses, one can find the enhancement of the efficiency of detector arrays [19], fabrication of optical components with non-Gaussian imaging properties [20], array illuminators for digital optical processing [21], sampling an optical wavefront for adaptive optics and Hartmann-Shack wavefront sensors [22–24], diffusers for LED backlight systems [25], and micro-sized object imaging [26].

2.2.3 Pyr-Array design

The third type of optical element consists of an array of 20 × 20 pyramidal elements imprinted in hardened steel with a pyramidal Vickers micro indenter separated by a distance of 50- and 100-μm pitch. Potential application of such structure can be in the so-called pyramid wavefront sensor, a device which employs refractive or reflective pyramid prism for adaptive optics and retinal imaging [27]. It was initially proposed by astronomers to measure aberrations introduced by the earth atmosphere [28]. It has since been used to measure the aberrations of the human eye [29] and within an adaptive optics loop to correct ocular aberrations [30]. More details on the design of this element can be found in references [27–30].

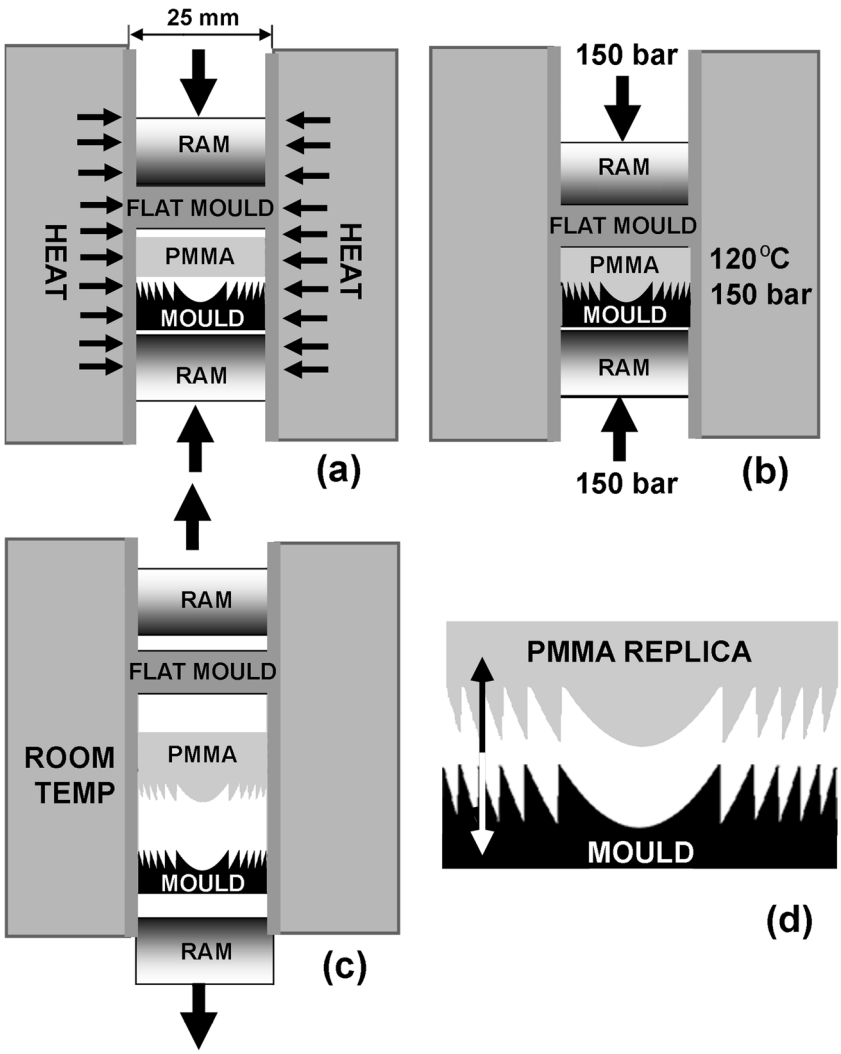

Fig. 6 Schematic diagram of the hot embossing apparatus used to replicate the optical elements onto PMMA. **a** Pre-heating, **b** hold, **c** cooling, and **d** de-molding

2.3 Nanometric and micrometric features machining for inserts mold making

This section is devoted to detail the fabrication of the mold inserts for the three proposed optical elements. Several machining conditions were tested on an electroless copper workpiece. The first part of the tests aimed to establish the replication fidelity of nanofeatures related to surface roughness generated by the machining process using diamond tools. A round-nose single crystal diamond tool geometry from Contour Fine Tooling® was used (C0.75mLG model: 763 μm nose radius, 0° rake angle, and 10° clearance angle). The cutting fluid used was Alkalisol 900, a synthetic oil with water soluble function-directed lubricate and cool mist formed on the workpiece/tool. The room temperature was kept constant at 21 ± 0.1 °C. Samples of commercially pure copper (electroless copper 99.9 %) were used in the test. The original Vickers micro-hardness of the sample was $Hv = 86$ kg$f$/mm^2. The workpiece size was 20 mm in diameter and 10 mm thickness.

The feedrate, f, and depth of cut, dc, were varied in order to find the most appropriated cutting condition to be used to fabricate the optical elements which generated the lowest root mean square surface roughness, R_{RMS}. Initially, f was varied from 5 to 20 μm/rev, keeping dc constant. From this set of conditions, the R_{RMS} behavior was measured, in order to choose the appropriated f condition to be used. The best result from this preliminary test (the value of f that minimized the value of R_{RMS} at dc constant) was used as the fixed value for a subsequent set of conditions at which dc was varied from 1 to 20 μm. The spindle speed was kept constant at 1000 rpm.

In the second part of the tests, the replication fidelity of micro features generated by the machining of Cyl-MLA and the Fr-Lens optical elements was evaluated. Considering the geometry of the proposed optical devices and their maximum surface relief to be machined, for practical reasons, $f = 1$ μm/rev was kept constant and dc was progressively increased,

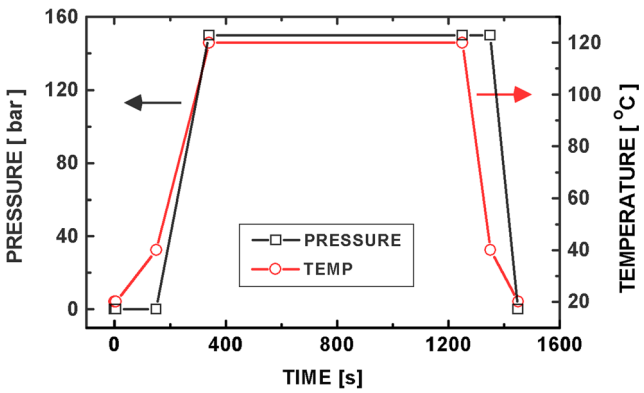

Fig. 7 Temperature and pressure temporal profiles during the replication process on PMMA

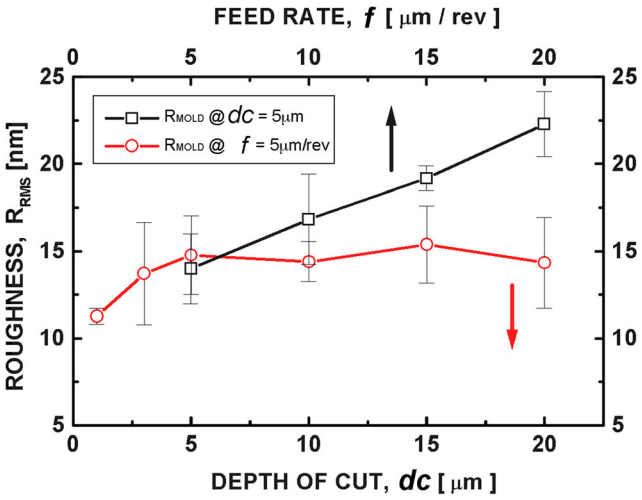

Fig. 8 Roughness behavior induced during machining of the mold insert fabrication (electroless copper) as a function of feedrate (f) and depth of cut (dc)

based on tool geometry and the machining strategy applied for the fabrication of the Cyl-MLA, as shown schematically in Fig. 3. Table 1 summarizes the experimental conditions and tool geometry used in the Cyl-MLA optical element mold insert fabrication.

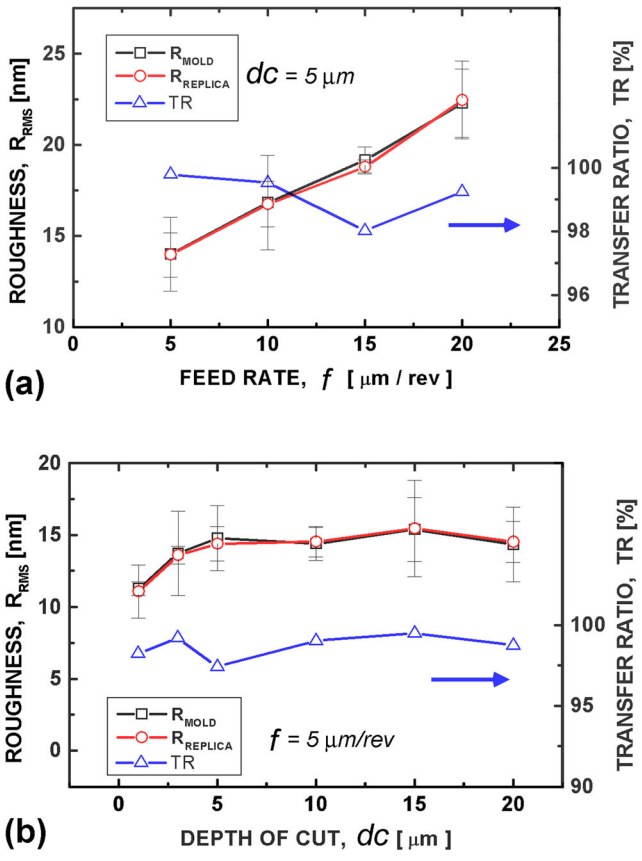

Fig. 9 Results for the surface quality and replication fidelity of PMMA replica obtained from the machined sample cut under different cutting conditions. **a** TR_{ROUGH} and R_{RMS} as a function of f and **b** TR_{ROUGH} and R_{RMS} as a function of dc

Considering the Fr-Lens device, the mold insert was also generated by diamond turning machining with a special geometry tool made of single crystal diamond designed for machining the Fresnel structures.

The employed machining strategy generated the Fresnel zones by means of a sequence of five passes varying *dc* values ($2 < dc < 10$ μm), and keeping $f = 1$ μm/rev, as schematically shown in Fig. 4a, b, shows a SEM micrograph of the single-point diamond half radius tool used to machine the Fresnel mold cavity.

This tool design allowed very sharp sidewalls to be machined while maintaining the required smooth machined surface. Table 2 summarizes the experimental conditions and tool geometry used in the machining for the Fr-Lens mold insert fabrication.

Considering the Pyr-Array optical element, its mold insert was obtained by imprinting in hardened steel with a computer-controlled pyramidal Vickers micro indenter. Figure 5 shows a schematic view of the indentation equipment, with the controlled parts, as well as the indentation strategy for the generation of the micro-pyramid array.

Several tests were performed and the best result was obtained for the conditions summarized by Table 3.

2.4 Replication process by hot embossing

Figure 6 shows the schematic diagram of the hot embossing apparatus used to replicate the optical elements on PMMA. The process sequence involves four steps: pre-heating, hold, cooling, and de-molding.

PMMA has a glass transition temperature of 105 °C [1] which is overwhelmed by the constant temperature achieved by the molding apparatus (120 °C). The pressing sequence is carried out in order to accommodate the polymer flowing, as graphically shown in Fig. 7. Replication tests were carried out in order to find what pressure would be more feasible to apply to the replication fidelity test. Best replication results within micro- and nanoscaling were obtained at 150-bar pressure. The increase in pressure did not reveal any improvement with respect to the replication quality.

Initially, the temperature of the mold is raised, at a rate of 0.13 °C/s, from room temperature (20.5 °C) until it reaches 40 °C, after 150 s. From this point, the temperature was further raised at a rate of 0.42 °C/s, reaching 120 °C after 340 s from the beginning of the process, and the pressure is constantly increased with a rate of 0.79 bar/s until it reaches 150 bar.

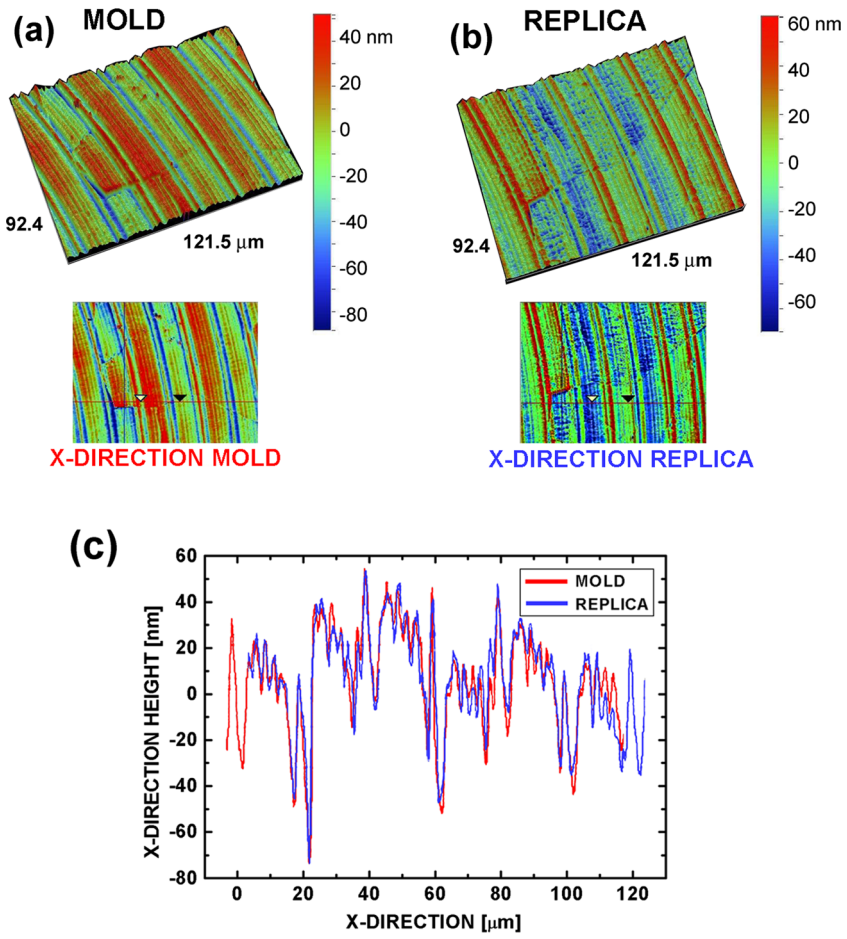

Fig. 10 Characterization of the flat part of the mold insert and replica from the machined sample under different cutting conditions. **a** 3D and 2D mappings of the mold insert, **b** 3D and 2D mappings of the PMMA replica, and **c** superimposed cross sections from the mold and replica in the *x*-direction. Cross section profiles were obtained, paying attention to get as exactly as possible the same path from mold and replica

The pressure applied was continuously checked and kept constant until the mold is released in order to avoid shrinking marks caused by the difference between the thermal expansion coefficients of the mold and the PMMA material.

3 Results and discussion

This section is devoted to present the results concerning the optical devices. First of all, the replication of nanofeatures will be presented and discussed. Secondly, the microscale feature replication fidelity will be presented considering the three optical elements studied. The parameters analyzed and measured were the dimensional agreement with respect to the design, the final optical quality of the mold insert as well as the PMMA replica, and replication fidelity of the hot embossing process.

Figure 8 summarizes these results from the machining test carried out in order to evaluate the replication fidelity of surface roughness obtained by machining of an electroless copper sample under different machining conditions. It was found that the lower the f and dc, the lower is the induced R_{RMS}. One can note that the surface roughness generated in the mold insert has a stronger dependence with f. The R_{RMS} remains approximately constant as a function of dc, and it scales linearly as a function of f.

In order to quantitatively evaluate the characteristics of the replication process at nanometer level, comparative measurements on the mold and replica, considering the R_{RMS} values, were carried out. To this end, a figure of merit called roughness transfer ratio, TR_{ROUGH}, was introduced, which is defined as

$$TR_{ROUGH} = 1 - \left\{ \frac{\left| R_{RMS}^{MOLD} - R_{RMS}^{REPLIC} \right|}{R_{RMS}^{MOLD}} \right\} \times 100 \quad (4)$$

where R_{RMS}^{MOLD} is the RMS roughness of the mold insert and R_{RMS}^{REPLIC} is the RMS roughness of the PMMA replica.

Figure 9 shows the results for the surface roughness and the transfer ratio considering the replication of the machined sample results presented in Fig. 8 by hot embossing replication

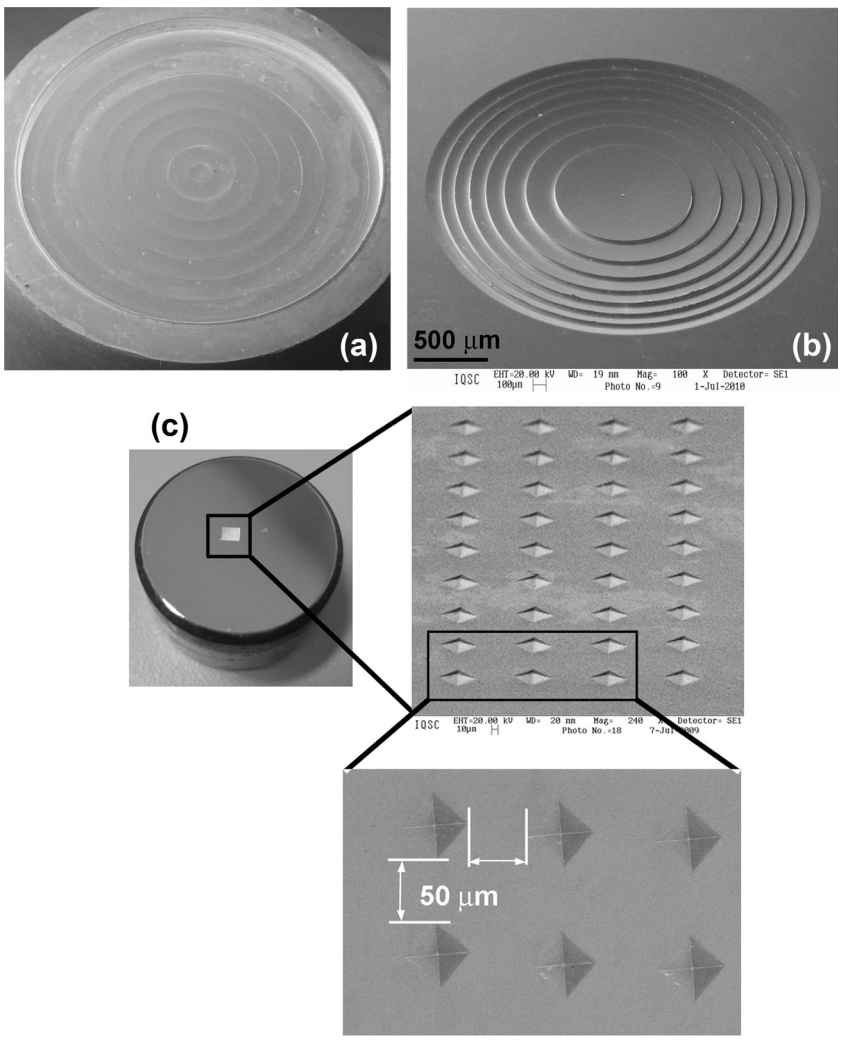

Fig. 11 Fabricated inserts mold. **a** Cyl-MLA: SEM micrograph of the mold insert on copper substrate; **b** Fr-Lens: SEM micrograph of the mold insert on copper substrate; **c** Pyr-Array: SEM micrographs of the hardened steel mold insert, showing the spacing of 50 μm between two imprints

process described in section 2.4. Figure 9a, b shows R_{RMS}^{MOLD}, R_{RMS}^{REPLIC}, and TR_{ROUGH}, as a function of f and dc, respectively.

Considering the replication process, one can note that the surface roughness induced in the PMMA replica follows the roughness of the mold insert. Taking the worst case in which the maximum value of R_{RMS} equals approximately 25 nm, and considering this device operating in the visible region of the spectrum, with an average wavelength of $\lambda = 500$ nm, one infers a ratio of approximately $R_{RMS} = (\lambda/20)$. This level of surface roughness is acceptable to be used in most visible range applications.

The difference in R_{RMS} between the machined sample and the replicated sample is as small as 1 nm. The measurements were made at matching points in the machined mold and replicated part. The results showed that even nanostructures generated by the material removal process, for example, crystal grain elastic recovery, were well replicated with differences in the nanometer range, which is within the vertical resolution of the profiler. Based upon these results, it is possible to assert that the machined nanometric features are replicated with high fidelity.

Figure 10 shows images from one of the cutting test condition and its replica on the PMMA.

Figure 10a, b shows the 3D and 2D mapping images from the machined sample and the PMMA replica, respectively. Figure 10c shows the cross section profiles of the mold insert and replica, performed in x-direction. The 2D and 3D scanning were performed at the same spot areas from the mold and from the replica counterpart. Cross section profiles were also obtained, paying attention to get as exactly as possible the same path from mold and replica. The cross sections were then superimposed in order to compare the topography from mold and replica and therefore evaluate the replication fidelity in the sub-micrometer scale.

It is worth mentioning that the profiles were replicated with high fidelity at nanometer range. The average difference between mold and replica was 3.6 nm within 120-nm peak-to-valley amplitude range, and x-direction scanning along 120 μm. This difference shows that even nanostructured features were well replicated. These features were generated by the material removal mechanism during surface formation, due to crystal grain elastic recovery.

Figure 11 shows the fabricated mold inserts for the three optical elements, ready to be used in the replication process onto PMMA. Figure 11a shows SEM micrograph of the Cyl-MLA mold insert on copper substrate after machining; Fig. 11b shows SEM micrograph of the aspheric Fr-Lens mold insert on copper substrate after machining; Fig. 11c shows SEM micrographs of the hardened steel mold insert used to imprint the Pyr-Array optical element, showing the spacing of 50 μm between two imprints.

3.1 Cyl-MLA results

Figure 12a, b shows a 3D views and cross section profiles of the Cyl-MLA optical element, for the machined mold insert and PMMA replica, respectively. One can note that the lens diameter and maximum height (sagitta) equals respectively to 497.7 and 6.47 μm for the mold and equals to 498 and 6.48 μm for the replica. These results are with acceptable agreement with the designed nominal values of 500 and 6.4 μm, respectively. The percentage variation between mold

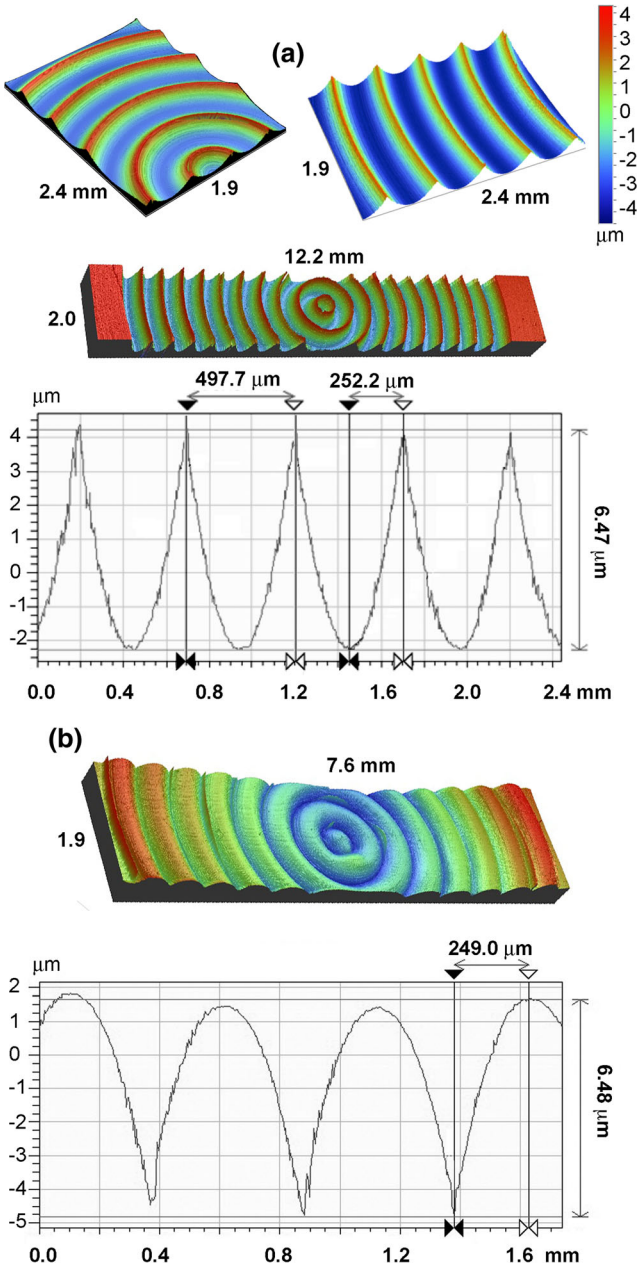

Fig. 12 Characterization of the Cyl-MLA optical element. **a** 3D views and cross section profile of the mold insert showing the lens diameter and maximum height and **b** 3D views and cross section profile of the PMMA replica showing the lens radius and maximum height

and replica with respect to mold dimensions are 0.06 % for the lens diameter and 0.15 % for the lens height.

3.2 Fr-Lens results

Figure 13 shows the results for the aspheric Fresnel lens mold and PMMA replica. Figure 13a, b shows the mold insert with a concave aspheric Fresnel profile. Figure 13c, d shows the 3D images and profile cross sections of PMMA replica with a convex profile, obtained by the hot embossing process described in section 2.4. The cross section profiles highlight the width of the second ring, $W_{P=2}$, of the Fresnel structure, as well as its maximum height $h_{\mathrm{MAX},P=2}$.

Concerning the mold insert, one can note the maximum height $h_{\mathrm{MAX},P=2}{}^{\mathrm{MOLD}} = 29.47$ μm and the second ring width $W_{P=2}{}^{\mathrm{MOLD}} = 221.41$ μm. Concerning the PMMA replica, one finds the maximum height $h_{\mathrm{MAX},P=2}{}^{\mathrm{REPLICA}} = 29.15$ μm and the second ring width $W_{P=2}{}^{\mathrm{REPLICA}} = 222.41$ μm. These results are with acceptable agreement with the designed nominal values. The percentage variation between mold and replica

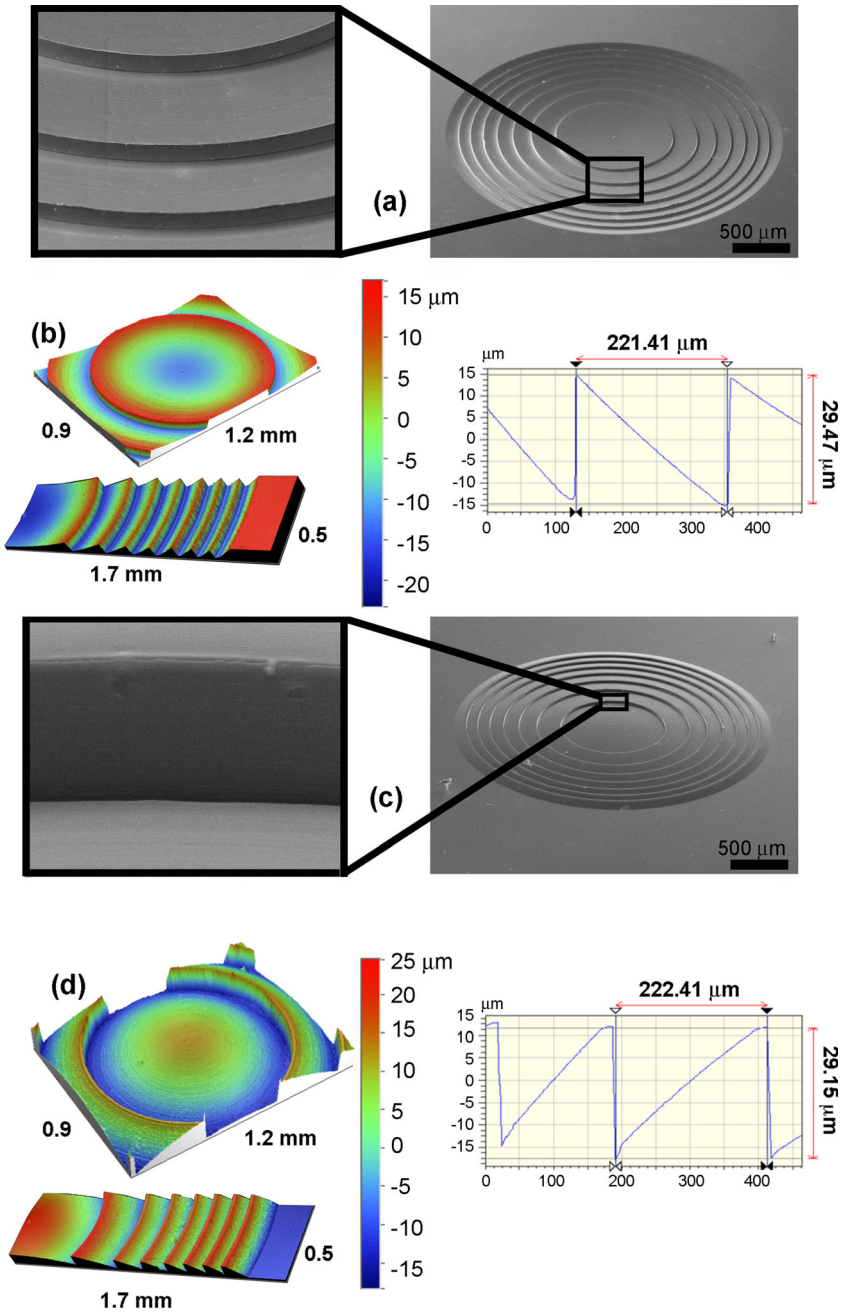

Fig. 13 Characterization of the aspheric Fresnel lens mold and replica. **a** SEM of the concave mold insert and **b** its respective 3D images and cross section profile; **c** SEM of the convex PMMA replica and **d** its respective 3D images and cross section profile

with respect to mold dimensions are 0.45 % for the ring width and 1.08 % for the lens height.

Considering the Fresnel lens, the replication process was also evaluated in terms of the dimensional variations of the replica with respect to the mold. To this end, two other figures of merit were introduced, namely, the height transfer ratio of the Fresnel structure, TR_{HEIGHT}, and the width transfer ratio of the Fresnel structure, TR_{WIDTH}, defined as the absolute difference between mold and replica characteristic dimensions, with respect to mold:

$$TR_{\mathrm{HEIGHT}} = \left\{1 - \frac{\left|h_{\mathrm{MAX},P}^{\mathrm{MOLD}} - h_{\mathrm{MAX},P}^{\mathrm{REPLIC}}\right|}{h_{\mathrm{MAX},P}^{\mathrm{MOLD}}}\right\} \times 100 \ , \quad (1 < P < 7) \tag{5}$$

$$TR_{\mathrm{WIDTH}} = \left\{1 - \frac{\left|W_P^{\mathrm{MOLD}} - W_P^{\mathrm{REPLIC}}\right|}{W_P^{\mathrm{MOLD}}}\right\} \times 100 \ , \quad (1 < P < 7) \tag{6}$$

where $h_{\mathrm{MAX},P}{}^{\mathrm{MOLD}}$ is the h_{MAX} of the Pth Fresnel zone (ring) of the mold insert, as define previously (Eq. 4), $h_{\mathrm{MAX},P}{}^{\mathrm{REPLIC}}$ is the h_{MAX} of the Pth ring of the PMMA replica, $W_P{}^{\mathrm{MOLD}}$ is the width of the Pth ring of the mold insert, and $W_P{}^{\mathrm{REPLIC}}$ is the width of the Pth ring of the PMMA replica. Both h_{MAX} and W are measured at its correspondent Pth zone.

Figure 14 shows $h_{\mathrm{MAX},P}{}^{\mathrm{MOLD}}$, $h_{\mathrm{MAX},P}{}^{\mathrm{REPLIC}}$, and TR_{HEIGHT} for each of the seven zones of the Fresnel lens. From Fig. 14a, one can note that h_{MAX} decreases slightly as the Fresnel annular zone location is farther from the center. This is expected due to the highest aspect ratio of the annular zone, which makes the machining of the mold insert with the employed tool more difficult. For all zones, TR_{HEIGHT} remains approximate constant between 99 and 100 %.

From Fig. 14b, one can note that TR_{WIDTH} decreases as a Fresnel zone approaches the periphery of the lens. This is also expected due to the higher aspect ratio of the higher order zones, which makes the penetration of melted PMMA during molding process difficult.

The RMS surface roughness was also evaluated and the same values as the previous device was found, i.e., a roughness level of $R_{\mathrm{RMS}} \sim (\lambda/20)$. This level os surface roughness is also acceptable to be used in most visible range applications. From the measurements of the annular distance and maximum height, one can note a very good agreement between cooper mold and PMMA replica. The high quality of the replication process is clear.

3.3 Pyr-Array results

Figure 15 shows the measured results for the pyramidal structure mold and PMMA replica, also made by means of an optical interferometric profiler.

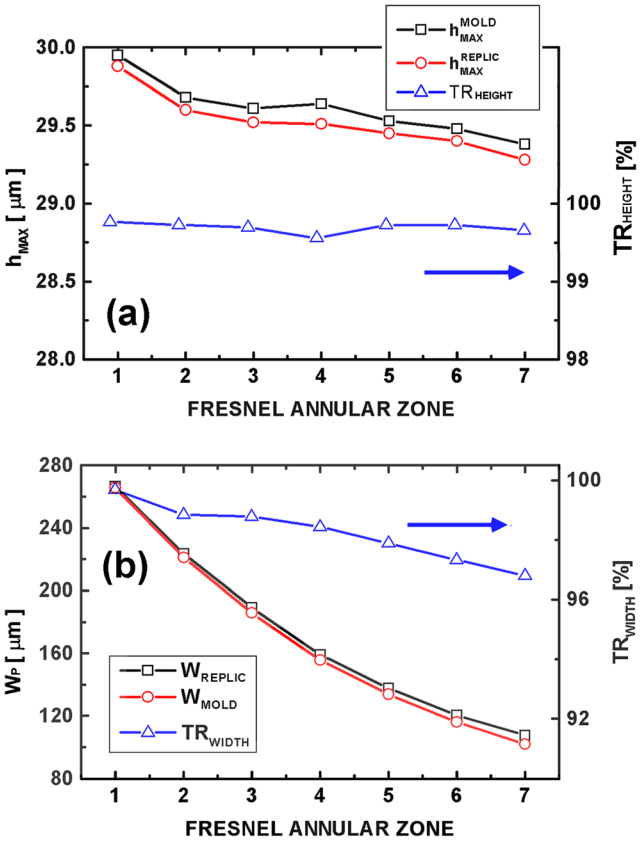

Fig. 14 Fresnel lens characterization as a function of Fresnel annular zones. **a** $h_{\mathrm{MAX},P}{}^{\mathrm{MOLD}}$, $h_{\mathrm{MAX},P}{}^{\mathrm{REPLIC}}$, and TR_{HEIGHT} as a function of Fresnel annular zones and **b** $W_P{}^{\mathrm{MOLD}}$, $W_P{}^{\mathrm{REPLIC}}$, and TR_{WIDTH} as a function of the Fresnel annular zones

Figure 15a shows pyramid images and diagonal cross section profile of the hard steel mold; Fig. 15b shows pyramid images and diagonal cross section profile of the PMMA replica. The cross sections indicate the half-diagonal sizes and the penetration depths of the mold and replica.

Concerning the mold insert, one can note the pyramid maximum height equals 6.37 µm and pyramid base half-diagonal equals 25.98 µm. Concerning the PMMA replica, one finds the pyramid maximum height equals 6.30 µm and pyramid base half-diagonal equals 25.93 µm. These results are with acceptable agreement with the designed nominal values of 25 µm for pyramid base half-diagonal and 6.3 µm for pyramid maximum height. The percentage variation between mold and replica with respect to mold dimensions are 1.09 % for the pyramid maximum height and 0.19 % for the pyramid base half-diagonal.

The R_{RMS} was also evaluated and a roughness level of $R_{\mathrm{RMS}} \sim (\lambda/10)$ was found. This surface quality was not as good as the Fresnel lens due to some defects present in the hard steel mold which have been replicated to the PMMA replica. Besides the defects, this level of surface roughness is still acceptable to be used in most visible range applications. An evaluation of TR_{HEIGHT} and TR_{ROUGH} for this device also

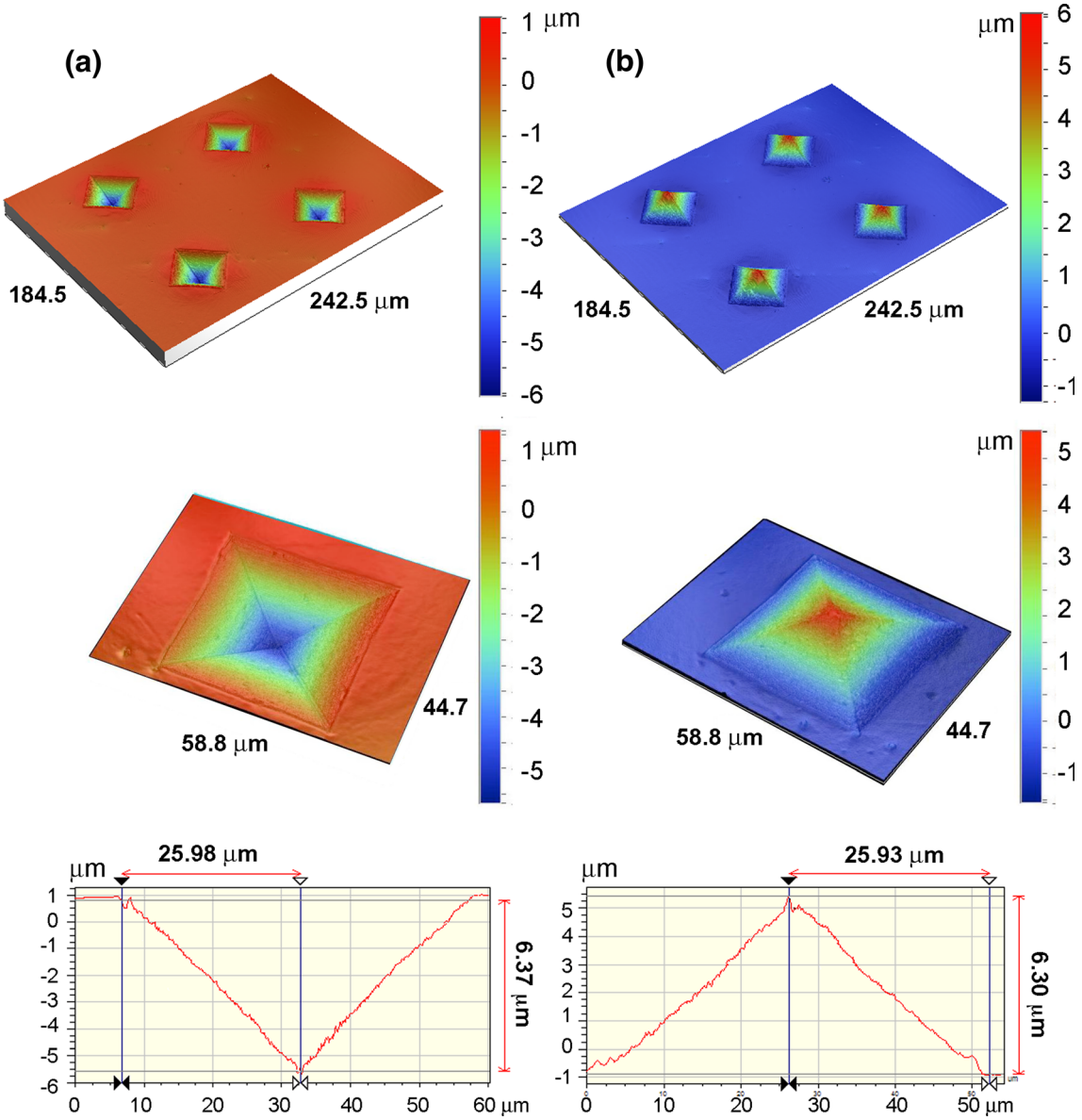

Fig. 15 Characterization of the pyramidal mold and replica. **a** 3D images and diagonal profile of the hard steel mold and **b** 3D images and diagonal profile of the replica on PMMA. Half-diagonal size and the penetration depth are indicated

shows the same level as for the other two previous optical elements presented, being within the range of 98 to 100 %.

4 Conclusions

This work presented the feasibility of the fabrication of several optical elements with micro- and millimeter-sizes by employing hot embossing process replication in PMMA. The mold inserts were fabricated by employing ultraprecision diamond-turning machining and computer-controlled mechanical indentation. All the devices were dimensionally characterized through the measurement of the degree of replication fidelity, as well as in terms of the resulting surface quality, considering both the mold inserts and PMMA replicas.

For all the presented optical elements, the resulting RMS surface roughness was lower than (λ/10), considering applications in the visible range of the spectrum. Concerning the replication fidelity, several transfer ratio functions, *TR*, were defined as the percentage difference between mold and replica, considering the particular characteristics of each different optical elements. For all the presented optical elements, the resulting *TR* was at least 96 %.

This level of replication fidelity enables one to replicate even nanostructured features generated by the material removal process during the mold insert fabrication, such as crystal grain elastic recovery. These features

were well replicated with differences in the range of few nanometers within the vertical resolution of the employed optical profiler technique.

Acknowledgments This work was supported by the Brazilian research financing agencies FAPESP – Fundação de Amparo a Pesquisa do Estado de São Paulo (Process No. 2008/53641-5), and CNPq – Conselho Nacional de Desenvolvimento Científico e Tecnológico (Process No. 472334/2008).

References

1. Herzig HP (1997) Micro-optics: elements, systems and applications. Taylor and Francis, Bristol, p 61
2. Hung KY, Chen YK, Huang SH, Shye DC (2010) Molding and hot forming techniques for fabricating plastic aspheric lenses with high blue-light transmittance. Microsyst Technol 16:1439–1444
3. Su Y, Shah J, Liwei L (2004) Implementation and analysis of polymeric microstructure replication by micro injection molding. J Micromech Microeng 14:415–422
4. Metwally K, Barriere T, Khan-Malek C (2016) Replication of micrometric and sub-micrometric structured surfaces using micro-injection and micro-injection compression moulding. Int J Adv Manuf Technol 83:779–789
5. Mosaddegh P, Angstadt DC (2008) Micron and sub-micron feature replication of amorphous polymers at elevated mold temperature without externally applied pressure. J Micromech Microeng (18)035036
6. Singh A, Metwally K, Michel G, Queste S, Robert L, Malek CK (2011) Injection moulding using an exchangeable Si mould insert. Micro Nanosyst 3:230–235
7. Shen YK, Chang HJ, Lin CT (2006) Study on optical properties of microstructure of lightguiding plate for micro injection molding and micro injection-compression molding. Mater Sci Forum 505–507: 229–234
8. Shan XC, Maeda R, Murakoshi Y (2003) Micro hot embossing for replication of microstructures. Jpn J Appl Phys 42:3859–3862
9. Lee BK, Kim DS, Kwon TH (2004) Replication of microlens arrays by injection molding. Microsyst Technol 10:531–535
10. Huang K (2008) Rapid replication of nanostructures made with a polymer using simple injection molding. J Appl Polym Sci 107: 497–500
11. Hattori S, Nagato K, Hamaguchi T, Nakao M (2010) Rapid injection molding of high-aspect-ratio nanostructures. Microelectron Eng 87(2010):1546–1549
12. Holger Becker H, Heim U (2000) Hot embossing as a method for the fabrication of polymer high aspect ratio structures. Sensors Actuators 83:130–135
13. Griffiths CA, Dimov SS, Brousseau EB, Packianather MS (2008) The finite element analysis of melt flow behaviour in micro-injection moulding. IMechE B: J Eng Manuf 222:1107–1118
14. Romankiw LT, Croll IM, Hatzakis M (1993) Think small: one day it may be worth a billion. Interface, Summer, p 17–57
15. Malacara-Hernández D, Malacara-Doblado D (2015) What is a Hartmann test? Appl Opt 54:9
16. Carvalho LA, Chamon W, Schor P, Castro JC (2006) Quantitative comparison of different-shaped wavefront sensors and preliminary results for defocus aberrations on a mechanical eye. Arq Bras Oftalmol 69(2):239–47
17. Goodman JW (1996) Introduction to Fourier optics, 2nd edn, chapter 4, p 63
18. Sinzinger S, Jahns Y (2003) Diffractive microoptics. In: Microoptics, 2nd edn, p 154-158
19. Seabra AC et al (2000) Increasing the optical coupling efficiency of planar photodetectors: electron beam writing of an integrated microlens array on top of an MSM device. International Topical Meeting on Optical Computing, Quebec, pp 890–894
20. Rees JD (1982) Non-Gaussian imaging properties of GRIN fiber lens arrays. Appl Opt 21(6):1009–1012
21. Goodman JW, Dias AR, Woody LM (1978) Fully parallel, highspeed incoherent optical method for performing discrete Fourier transformation. Opt Lett 2(1):1–3
22. Monteiro DWL (2002) CMOS-based integrated wavefront sensor. Delft University Press, Delft, p 78
23. Artzner GE (1992) Microlens arrays for Shack-Hartmann wavefront sensors. Opt Eng 31(6):1311–1322
24. Yoon GY et al (1996) Shack Hartmann wave-front measurement with a large F-number plastic microlens array. Appl Opt 35(1):188–192
25. Chang SI et al (2006) Microlens array diffuser for a light-emitting diode backlight system. Opt Lett 31(20):3016–3018
26. Tripathi A, Chronis N (2011) A doublet microlens array for imaging micron-sized objects. J Micromech Microeng 21(10):105024
27. Aina W, Jun Y, Dongmei C, Hao R (2010) Design and fabrication of a pyramid wavefront sensor. Opt Eng 49(7):073401
28. Ragazzoni R (1996) Pupil plane wavefront sensing with an oscillating prism. J Mod Opt 43:289
29. Iglesias I, Ragazzoni R, Julien Y, Artal P (2002) Extended source pyramid wave-front sensor for the human eye. Opt Express 10:419
30. Chamot SR, Dainty C, Esposito S (2006) Adaptive optics for ophthalmic applications using a pyramid wavefront sensor. Opt Express 14:518, **2525**